Refining the shallow slip deficit

Xiaohua Xu,[1] Xiaopeng Tong,[2] David T. Sandwell,[1] Christopher W.D. Milliner,[3] James F. Dolan,[3] James Hollingsworth,[4] Sebastien Leprince[5] and Francois Ayoub[5]

[1]*Institute of Geophysics and Planetary Physics, Scripps Institution of Oceanography, La Jolla, CA 92037, USA. E-mail: sddyxxh@gmail.com*
[2]*Department of Earth and Space Sciences, University of Washington, Seattle, WA 98115, USA*
[3]*Department of Earth Sciences, University of Southern California, Los Angeles, CA, USA*
[4]*Arup, London, United Kingdom*
[5]*Division of Geological and Planetary Science, California Institute of Technology, Pasadena, CA, USA*

SUMMARY

Geodetic slip inversions for three major ($M_w > 7$) strike-slip earthquakes (1992 Landers, 1999 Hector Mine and 2010 El Mayor–Cucapah) show a 15–60 per cent reduction in slip near the surface (depth < 2 km) relative to the slip at deeper depths (4–6 km). This significant difference between surface coseismic slip and slip at depth has been termed the shallow slip deficit (SSD). The large magnitude of this deficit has been an enigma since it cannot be explained by shallow creep during the interseismic period or by triggered slip from nearby earthquakes. One potential explanation for the SSD is that the previous geodetic inversions lack data coverage close to surface rupture such that the shallow portions of the slip models are poorly resolved and generally underestimated. In this study, we improve the static coseismic slip inversion for these three earthquakes, especially at shallow depths, by: (1) including data capturing the near-fault deformation from optical imagery and SAR azimuth offsets; (2) refining the interferometric synthetic aperture radar processing with non-boxcar phase filtering, model-dependent range corrections, more complete phase unwrapping by SNAPHU (Statistical Non-linear Approach for Phase Unwrapping) assuming a maximum discontinuity and an on-fault correlation mask; (3) using more detailed, geologically constrained fault geometries and (4) incorporating additional campaign global positioning system (GPS) data. The refined slip models result in much smaller SSDs of 3–19 per cent. We suspect that the remaining minor SSD for these earthquakes likely reflects a combination of our elastic model's inability to fully account for near-surface deformation, which will render our estimates of shallow slip minima, and potentially small amounts of interseismic fault creep or triggered slip, which could 'make up' a small percentages of the coseismic SSD during the interseismic period. Our results indicate that it is imperative that slip inversions include accurate measurements of near-fault surface deformation to reliably constrain spatial patterns of slip during major strike-slip earthquakes.

Key words: Satellite geodesy; Seismic cycle; Radar interferometry.

1 INTRODUCTION

Maps of relative, line-of-sight (LOS), surface deformation from interferometric synthetic aperture radar (InSAR) combined with absolute vector measurements from point global positioning system (GPS) data have enabled the mapping of the 3-D surface displacement for many large earthquakes (Fialko *et al.* 2001). If the fault plane is well defined by geological field mapping and aftershocks, then elastic models can be used to invert for the spatial variations of slip at depth. The equations relating slip at depth to surface deformation include an upward continuation term that dramatically attenuates the rupture signal at wavelengths smaller than the depth, so

model resolution generally decreases exponentially with increasing depth (Fig. S5). Thus, slip at shallow depths is well resolved whereas the spatial variations in deeper slip are poorly resolved. This poor resolution, combined with a smoothness constraint, results in a spatially smooth slip model at the base of the seismogenic zone (Tong *et al.* 2010). By using combined InSAR and GPS data, detailed slip inversions have been performed for several large strike-slip earthquakes in southern and Baja California, including the M_w7.3 Landers, M_w7.1 Hector Mine and the M_w7.2 El Mayor–Cucapah. The previous slip models for these earthquakes share a common attribute, in that their cumulative along-strike slip is largest between 2 and 6 km depth, with a 15–60 per cent reduction in slip at shallower
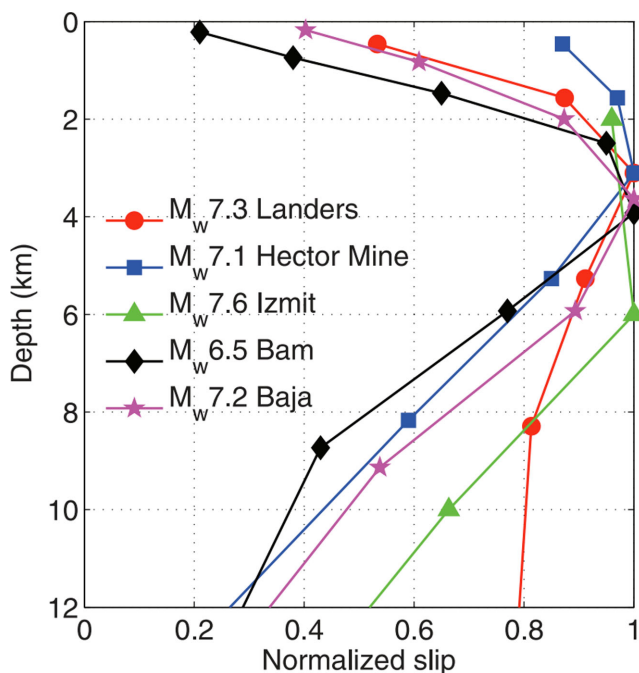
Figure 1. Distribution of cumulative coseismic slip for several large ($M_w > 7$) strike-slip earthquakes (Fialko *et al.* 2005, 2010). The cumulative coseismic slip is computed by integrating the strike-slip along strike. Horizontal axis represents normalized cumulative strike-slip.

depth (Fialko *et al.* 2005, 2010; Fig. 1). This feature is called the shallow slip deficit (SSD). When averaged over many earthquake cycles, the slip on a major fault should be uniform with depth and equal to the sum of the co-, post- and interseismic slip (Reid 1910; Tse & Rice 1986). The reduction in coseismic slip at the base of the seismogenic zone is explained by post- and interseismic slip. Near the surface, however, there is not enough steady interseismic creep or triggered slip to account for the observed SSD (Wei *et al.* 2009; Kaneko *et al.* 2015). The assessment and understanding of this SSD is important for palaeoearthquake magnitude estimation, geologists' mapping of surface coseismic slip after earthquakes and understanding the relation between surface rupture and slip at depth (Dolan & Haravitch 2014). It is also crucial in predicting strong ground motion and is thus critically important for accurate seismic hazard evaluation (Pitarka *et al.* 2009).

Previous studies have investigated physical processes to explain the SSD, but can only account for about a 15 per cent reduction in shallow slip by distributed deformation of the uppermost few kilometres surrounding the fault (Kaneko & Fialko 2011). Seismic imaging and geological mapping show the uppermost few kilometres of the crust above a strike-slip fault has 'V-shaped damage zone' having a locally reduced seismic velocity (Zhang *et al.* 2009). In addition, thick sediments (greater than 2 km) promote velocity strengthening behaviour, which has been proposed to result in shallow creep (Rice & Tse 1986). These processes suggest that inelastic off-fault deformation could explain a maximum coseismic slip deficit of about 15 per cent. However, compared to the observed 46 per cent surface slip deficit in Landers earthquake and 60 per cent in El Mayor–Cucapah earthquake (Fialko *et al.* 2005, 2010), this small amount is insufficient to explain the entire SSD.

Here we investigate whether the SSD is largely an artefact due to incomplete data coverage close to the rupture zone for 1992 Landers, 1999 Hector Mine and 2010 El Mayor–Cucapah earthquakes, all of which share similar tectonic settings (Fig. 2). These major ruptures, each of which exhibited a large SSD, also had large near-fault

ground motions and accelerations that caused strong decorrelation of the radar interferograms, making the exact near-fault measurement of surface deformation impossible. We first use inversions of synthetic InSAR data, with a variety of near-fault data gaps, to show that poor coverage of the near-fault surface deformation pattern can explain a significant part of the observed SSD. We then assemble additional near-fault deformation data from optical image analysis, better geological mapping of the fault trace, more refined InSAR data processing and more complete GPS data coverage for all three of these major strike-slip ruptures and invert for the slip at depth. We show that much smaller SSDs are consistent with all the observations and discuss possible explanations for the remaining minor SSDs.

2 SYNTHETIC TEST

To understand how a lack of near-fault data coverage could result in an underestimation of the shallow slip, we performed two synthetic tests. We constructed a uniform elastic half-space model that consists of a 30-km-long and 20-km-wide fault placed at a $150°$ strike and $65°$ dip (Fig. 3a). The slip along the fault varies as a Gaussian function tapering to zero towards the ends of the fault trace. The cumulative slip along strike is 60 m km for each layer down to a depth of 8.2 km where the slip goes to zero (9 km width on the fault plane). From the forward model, we generated the surface displacement field, and added Gaussian noise that is 2 per cent of the local signal amplitude. We then performed two inversions with two different-sized data gaps around the fault—a small 2-km-wide, 32-km-long elliptical gap and a larger 10-km-wide and 32-km-long elliptical gap (Fig. 3b). Inversions were carried out using the exact fault geometry, a non-negative strike-slip constraint and a gradient smoothing constraint. In both cases, the lower part of the model (Figs 3c and d) had a more gradual reduction in slip than the near-step input. In addition, they both showed an overestimate of slip at intermediate depth (3–5 km). The case with the small data gap, showed a reduction of surface slip with respect to the peak slip of 5 per cent while the case with the large data gap had a 18 per cent reduction of surface slip with respect to the peak (Figs 3e and f). Interestingly, for the model with the wide gap, most of this apparent SSD is not due to a slip mismatch at the surface, but due to an overestimate of slip at 4 km. An additional test with full data coverage was done (Fig. S4), but no significant difference was found in the inverted slip compared to the 2 km gapped case. This experiment demonstrates that the missing near-fault data, combined with a smoothed, non-negative inversion, may result in a lower surface slip relative to the slip in the centre of the seismogenic zone. These synthetic tests demonstrate that near-fault data are necessary in order to reliably quantify near-surface slip.

3 DATA PREPARATION

Our reanalysis of the SSD is based on improved data coverage as well as improved analysis methods for the three large strike-slip earthquakes in southern and Baja California (the $M_w = 7.3$ Landers, the $M_w = 7.1$ Hector Mine and the $M_w = 7.2$ El Mayor–Cucapah). We begin by assembling near-fault optical imagery data of repeated images from aircraft (1 m ground resolution) as well as the SPOT satellite (10 m ground resolution). We then reanalyse all the interferometry from these three earthquakes using improved non-boxcar (i.e. non-multilook) filters and better phase unwrapping close to the rupture by explicitly allowing for a phase discontinuity (Chen & Zebker 2001). Finally, we use all available continuous and
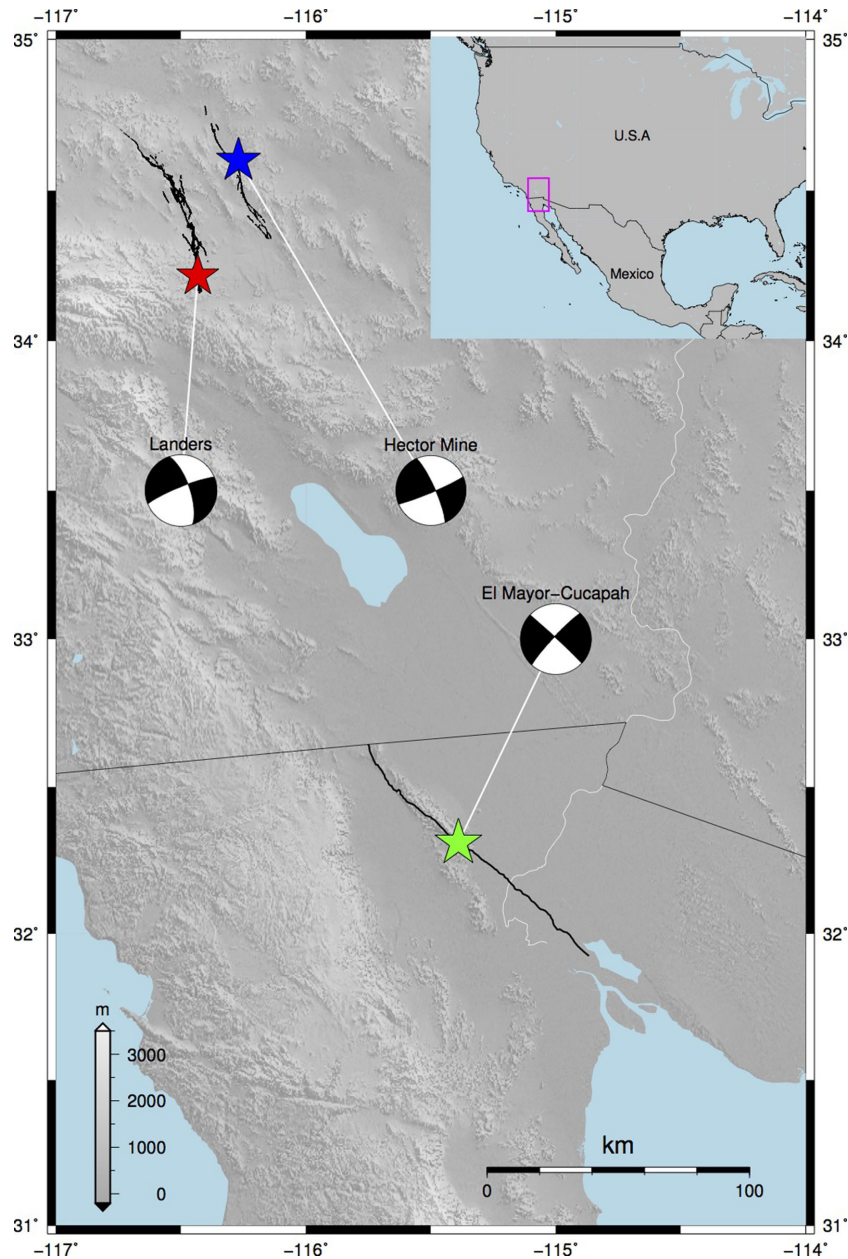
Figure 2. Tectonic setting of the three major strike-slip earthquakes in southern and Baja California. Stars represent epicentres of earthquakes, with beach balls denote the centroid moment tensor solutions (http://www.globalcmt.org).

campaign vector GPS data to better constrain the slip in the deeper parts of the ruptures.

3.1 Optical imagery data

We assembled near-fault optical imagery data of repeated images from aircraft as well as the SPOT satellite (Hollingsworth *et al.* 2012). We assembled high-resolution, National Aerial Photography Programme photographs (1 m ground resolution, compared to 4 m for InSAR), purchased from the USGS (http://earthexplorer.usgs.gov) to provide better constraints on surface deformation patterns close to the fault (Milliner *et al.* 2015). Images acquired prior to the earthquakes were correlated with images acquired after the earthquakes using the COSI-Corr software

(Leprince *et al.* 2007). To produce correlation maps that accurately constrain the ground deformation pattern, the input aerial photographs must be precisely orthorectified and coregistered before correlation. The COSI-Corr procedure allows for accurate orthorectification of images by taking into account the topography using a 10 m, national elevation data set, digital elevation model, the internal camera geometry using a camera calibration report and the exterior orientation (look angle and altitude) determined from ground control points (Ayoub *et al.* 2009). The pre-and post-event photographs were coregistered by constructing a relative mapping between image pairs using tie points that relate common features that were observable in both the pre- and post-earthquake images. To correlate the images, we used a multiscale sliding window size (64 and 32 pixels) with a 6-pixel step, which from multiple tests were found to be the optimal correlation parameters (Milliner *et al.*

(a)

(b)

(c)

(d)

(e)

(f)
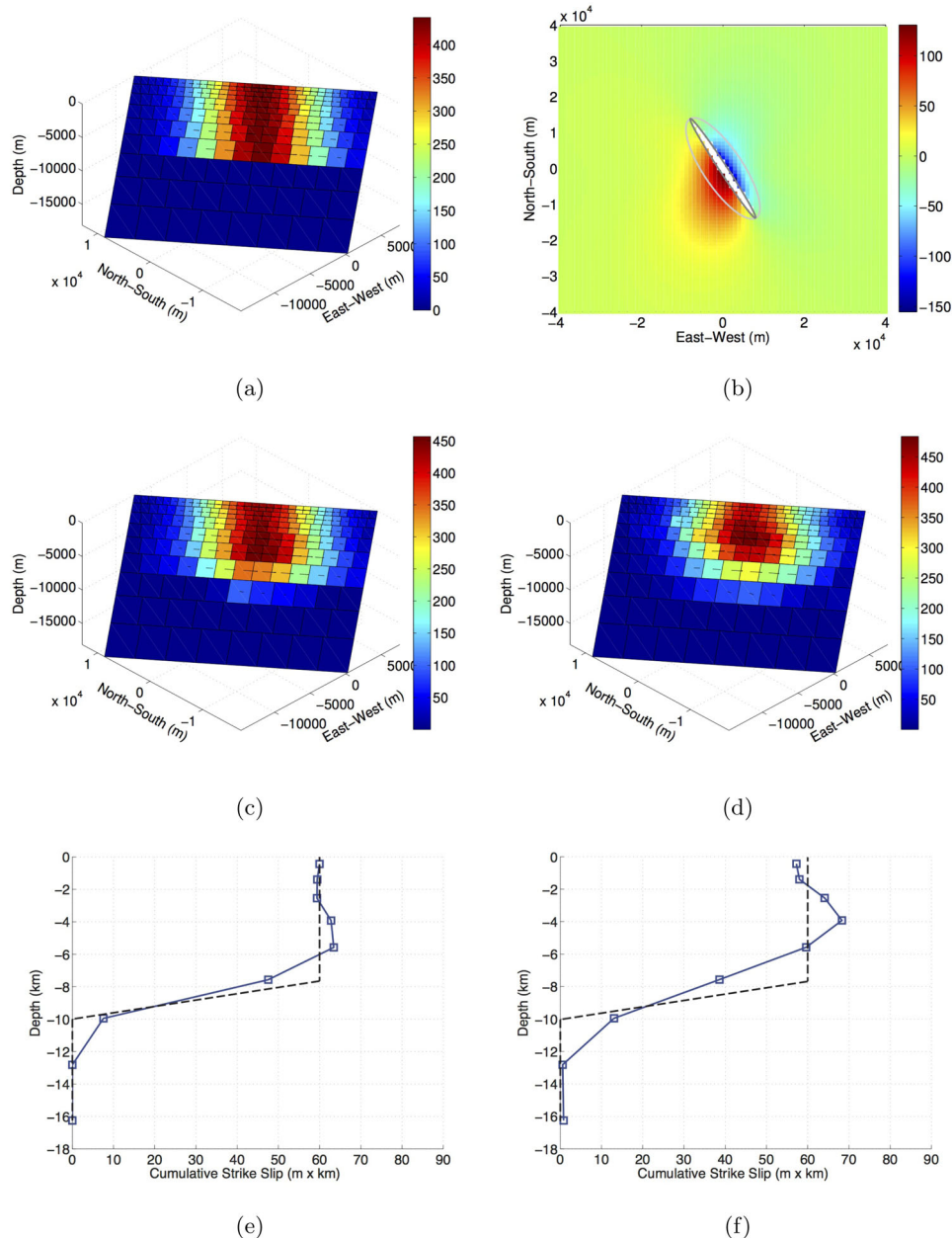
Figure 3. Synthetic test showing shallow slip deficit caused by missing near-fault data. (a) is the input model and (b) is the surface observations along north–south direction (part of the synthetic data used) generated from input slip model with different amount of missing data close to fault. Dark grey ellipse represents the thin mask used and light grey ellipse represents the wide mask used. (c) and (d) are inversion results from data in (b) with 2 per cent local noise being added; (c) corresponds to inversion with thin data mask while (d) corresponds to wide data mask. The colour represents strike-slip and the arrows represent total slip for each patch. (e) and (f) are cumulative strike-slip versus depth for models (c) and (d) and the dash line represents the cumulative strike-slip versus depth for the input model.

2015). This process yields two displacement maps, representing pixel motion in the east–west and north–south horizontal directions (Fig. 3). This methodology allows for detection of pixel shifts down to an accuracy of 1/10th the size of the input image pixel dimension, which is related to the image texture and degree of temporal decorrelation (Michel & Avouac 2006; Leprince *et al.* 2007; Ayoub *et al.* 2009).

To measure the total surface displacement across the entire width of surface deformation, we used stacked profiles oriented perpendicular to the fault strike (Milliner *et al.* 2015). Specifically, we used profiles that ranged from 1 to 2 km in length (perpendicular to fault) that were stacked over a 138 m, along-strike length

(i.e. fault parallel), which allows for suppression of noise. We applied a linear regression to the observed deformation signal on either side of the fault and the relative offset of the regressions defines the total displacement accommodated across the entire fault zone. Thus, the COSI-Corr displacement value includes both the localized, on-fault displacement that occurs on the primary fault strand, as well as any off-fault, distributed inelastic shear accommodated via a range of physical processes (Milliner *et al.* 2015; Fig. 4). Our surface offset estimates for these earthquakes are derived from the COSI-Corr analysis of aerial images for the Landers earthquake and of SPOT images for the Hector Mine and the El Mayor–Cucapah earthquakes. Subsampling and
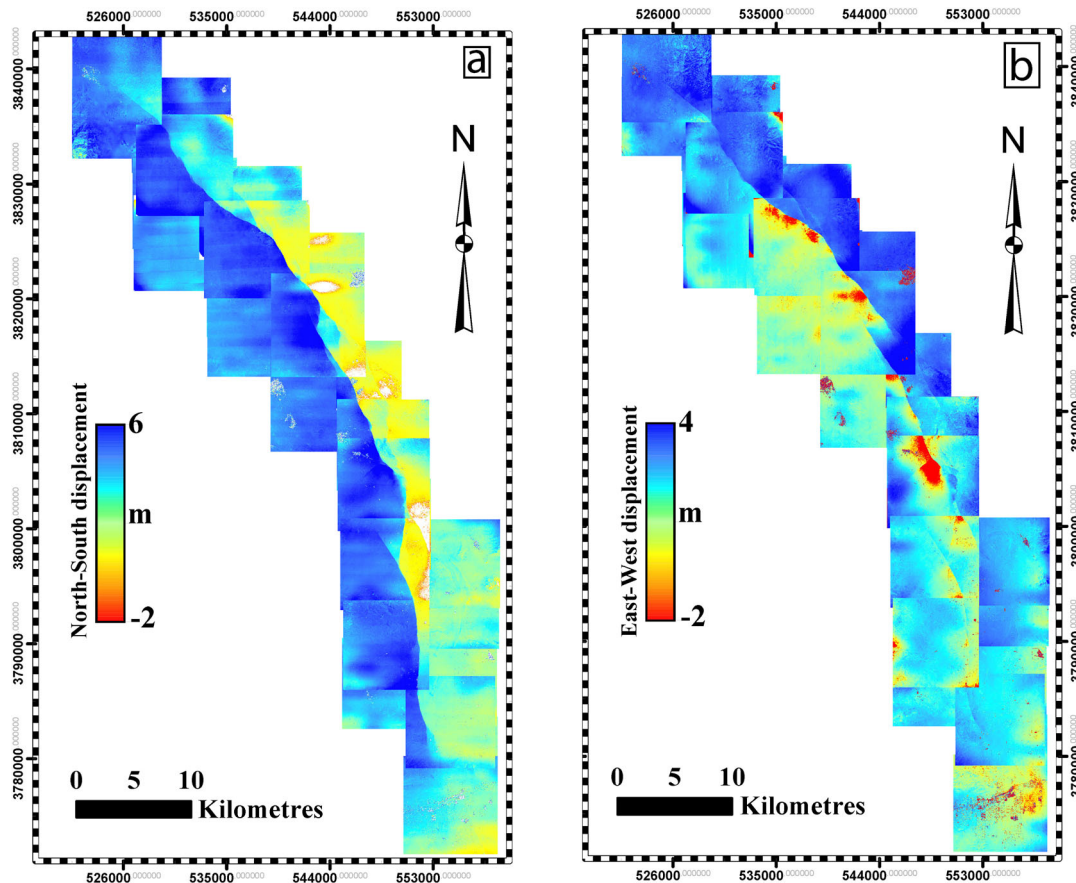
Figure 4. COSI-Corr processed aerial image from National Aerial Photography Programme of the 1992 Landers rupture. On the left is the north–south component of the surface deformation and on the right is the east–west component.
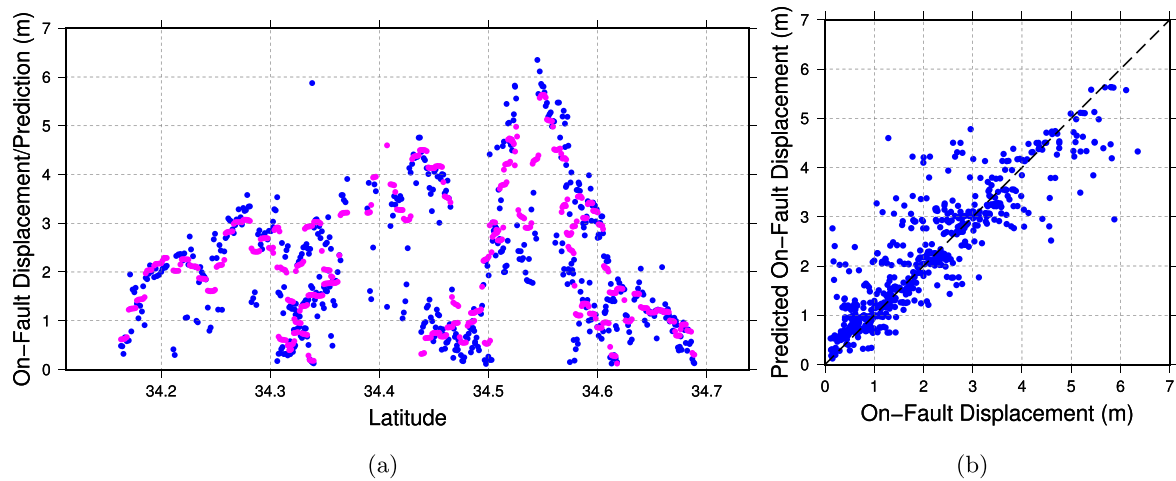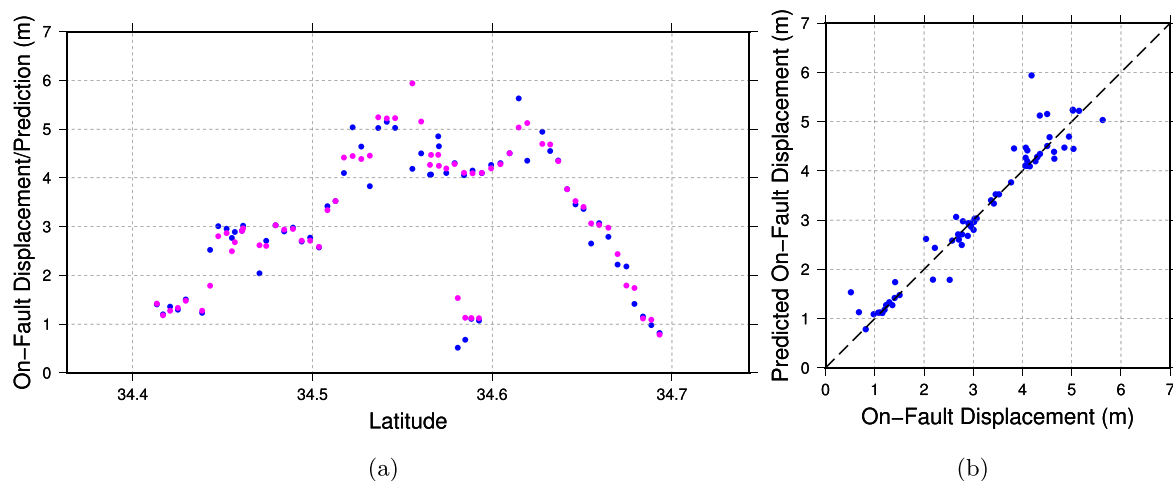

Figure 5. Fault offset from NAPP image COSI-Corr and prediction from our model for the 1992 Landers earthquake. (a) Blue dots being estimation from NAPP image, magenta dots are predicted offset at the same position on fault from our best-fitting model. (b) Comparison between fault offset and model prediction.

projection were made for these data subjecting to our models' traces, in order to assemble across-fault offset data set for inversions (Figs 5–7).

3.2 InSAR data

Repeat-pass interferometry spanning an earthquake provides very high spatial resolution coverage for the LOS displacement between any two points in the interferogram (Massonnet *et al.* 1993, 1994; Zebker *et al.* 1994). There are two main error sources in the analyses of these data. First, the large spatial scale motion (>40 km) can be contaminated by orbital trends and large-scale atmospheric and ionospheric phase delays. We dealt this during the inversion by including mean and trend parameters in the inversion to absorb the error (Simons *et al.* 2002). The second error source is related to phase unwrapping, especially close to the rupture where phase

Figure 6. Fault offset from NAPP image COSI-Corr and prediction from our model for the 1999 Hector Mine earthquake. (a) Blue dots being estimation from NAPP image, magenta dots are predicted fault offset at the same position on fault from our best-fitting model. (b) Comparison between fault offset and model prediction.
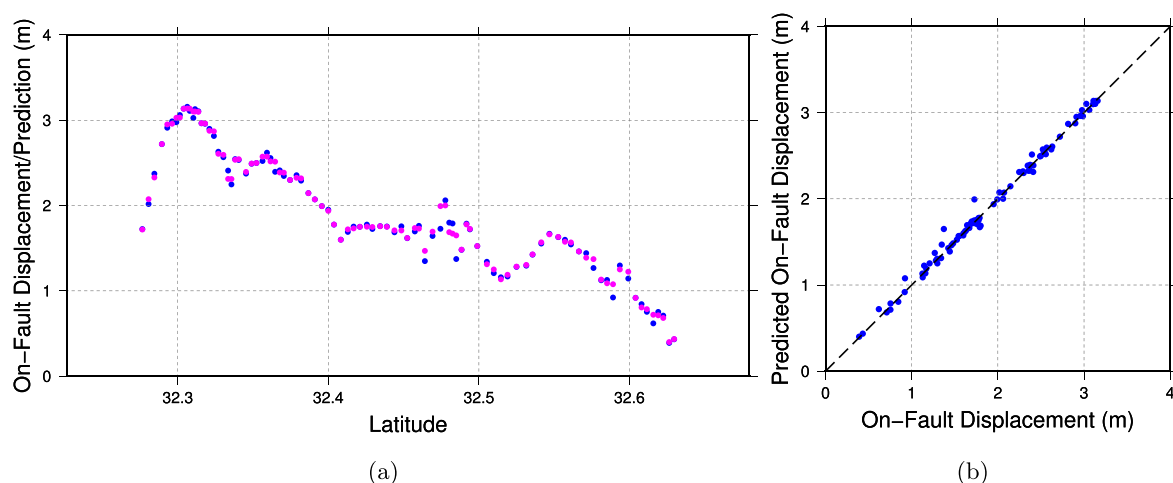
Figure 7. Fault offset from SPOT image COSI-Corr and prediction from our model for the 2010 El Mayor–Cucapah earthquake. (a) Blue dots being estimation from SOPT image, magenta dots are predicted fault offset at the same position on fault from our best-fitting model. (b) Comparison between fault offset and model prediction.

gradients are large and the InSAR coherence is low due to surface disruption from the strong ground accelerations. We increased the accuracy and coverage of the phase unwrapping close to the fault by two improvements in the processing. The first is related to the filtering of the interferogram. Previous studies have used a multilook filter (i.e. a boxcar average) (Simons & Rosen 2007) to suppress phase noise. However, in regions where the phase gradient approaches 2π per pixel, the spectral leakage of this filter will increase the phase noise. We have replaced the boxcar with a narrow Gaussian filter to recovered more phase data in the high gradient regions (Huang & Gendersen 1997; Sandwell & Price 1998). The optimal cut-off wavelength of the low-pass filter depends on the coherence of the interferogram. For the higher quality interferograms (e.g. Hector Mine descending pair with average correlation being 0.69), we used a filter with a 0.5 gain at a half-wavelength of 50 m while for other, more poorly correlated interferograms (e.g. Landers descending pair with average correlation being 0.22), a wider filter was used (0.5 gain at a half-wavelength of 100 m).

The second main improvement in our near-fault InSAR analysis is related to recent improvements in phase unwrapping methods. Chen & Zebker (2001) developed a method using Statistical-

cost Network-flow Algorithm for Phase Unwrapping (SNAPHU), which constructs a generalized cost function solving for a maximum a posterior probability estimation that approximates an L_0 solution for minimizing the phase gradient differences between wrapped and unwrapped phase. This L_0 norm solution is in accordance with the assumption that the total length of the discontinuity in the deformation field should be as short as possible. Besides, the algorithm also explicitly includes a maximum phase discontinuity parameter that allows for a sharp phase change across the discontinuity.

We optimized and tested the ability of this unwrapping algorithm to accurately recover phase near the fault by varying the discontinuity parameter (DEFOMAX) and also constructing a near-fault decorrelation mask (Fig. S3). The decorrelation mask provided information on the region where a phase discontinuity should exist and the discontinuity parameter specifies the maximum size of the phase discontinuity across the rupture. We systematically increased the assumed discontinuity value from 0 to 100 cycles of radians (i.e. a large enough value for significant rupture, approximately 89 cm for C band and 376 cm for L band). In addition, we carefully perturbed the width of the masked area. The optimal

(a)

(b)

(c)
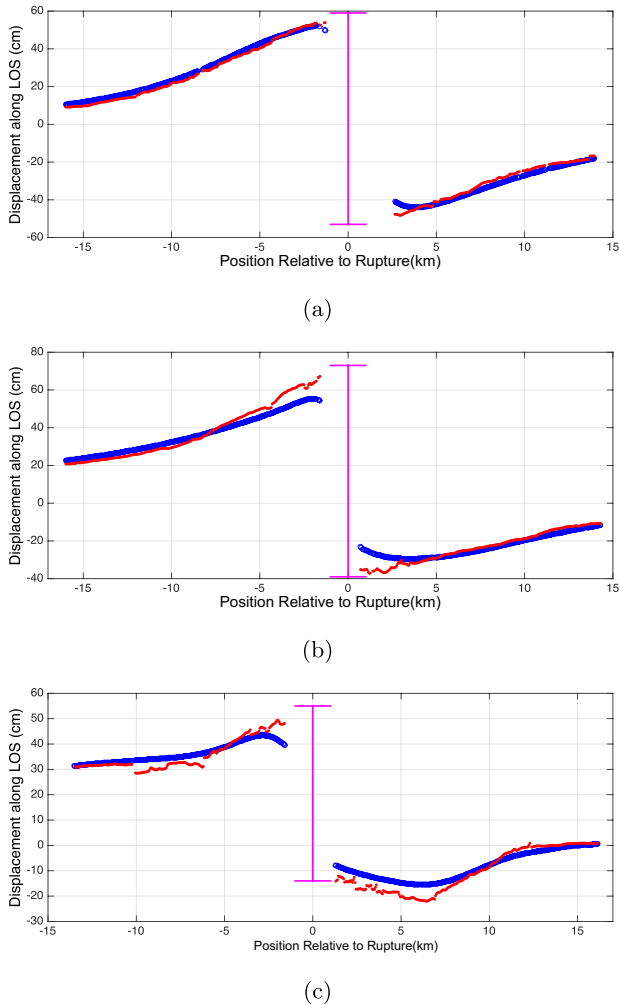
Figure 8. Comparison between previous model (Fialko 2004) prediction and our new unwrapped LOS displacement for the 1992 Landers earthquake. The blue circles are model prediction from previous study and the red dots are new unwrapped displacement field. The vertical magenta line is the estimated fault offset being placed at the fault position. The gap in between are segments being masked due to its low unwrapping reliability.

discontinuity value and fault mask width were established for each interferogram through visual inspection, and the most unstable part of the interferogram were masked. Typically the mask width is about 0.5 km for a well-correlated interferogram and 1.5 km for a poorly correlated interferogram and the assumed maximum discontinuity varies depending on the look angle and the magnitude of the rupture.

To assess the accuracy of the new unwrapping method, we performed a more detailed evaluation for the Landers rupture area. We compared the LOS deformation field on three profiles along with the prediction from a previous model (Fialko 2004) and the fault offset estimation from high-resolution optical image pixel tracking (Fig. 8). The results show a good agreement between the new unwrapped phase (red dots) and the COSI-Corr estimates (magenta vertical lines), whereas the previous model's prediction shows a significant discrepancy near the fault. This improvement in rear-fault phase unwrapping combined with the COSI-Corr measurements of the surface deformation pattern yields much improved estimates of total slip. The inclusion of such information about near-fault surface deformation is of critical importance for estimating coseismic shallow in the uppermost few kilometres of seismic ruptures.

The new filtering and phase unwrapping was performed on the following interferograms spanning the three major earthquakes: (1) Landers 1992 June 24—C-band ERS1 data, (2) Hector Mine 1999 October 16—C-band ERS2 data, (3) El Mayor–Cucapah 2010 April 4–Both C-band ENVISAT data and L-band ALOS data were used (Table 1 and Figs 9–11). These data sets are subsampled according to the curvature of the displacement field and different weights are pre-assigned before they are applied to our inversion, according to the sampling area (Simons *et al.* 2002).

3.3 GPS data

Unlike InSAR data which sometimes have significant orbital errors and are subject to atmospheric noise, the GPS data are usually more accurate, especially over wavelengths greater than 40 km. These less-dense but more accurate data help to constrain the slip on the deeper parts of the model. Moreover, since the 1992 Landers and 1999 Hector Mine earthquakes, additional campaign GPS data have been collected, which improves spatial coverage with respect to the data coverage used in the original slip-model publications. We used data from 82 GPS stations for the 1992 Landers earthquake (Bock *et al.* 1993; Fig. 12) and 77 GPS stations for the 1999 Hector Mine earthquake (Agnew *et al.* 2002; Fig. 13). For the 2010 El Mayor–Cucapah earthquake, we used observations of 158 GPS stations from both the Plate Boundary Observatory and the Centro de Investigacion Científica y de Educacion Superior de Ensenada (CICESE) network (Fig. 14). Even though the near-field measurements for the El Mayor–Cucapah earthquake are concentrated on one side of the fault, they provide an important constraint on the coseismic slip pattern. The weights for the inversion are pre-assigned according to the uncertainty in each observation.

Table 1. InSAR data acquisitions used for three major strike-slip earthquakes in Baja California.

| Earthquake	Satellite	Track	Master acquisition date	Repeat acquisition date	B_P (m)
Landers	ERS1	399 D	1992 April 24	1992 July 3	−344.63
1992 June 24		349 A	1992 May 26	1992 June 30	356.90
Hector Mine	ERS2	127 D	1998 September 15	1998 October 20	−16.05
1999 October 16		77 A	1999 November 12	1999 November 21	59.88
El Mayor–Cucapah	ENVISAT	77 A	2010 February 21	2010 March 28	−75.12
2010 April 4		306 A	2010 March 9	2010 April 13	244.39
		84 D	2010 March 28	2010 May 2	−87.98
	ALOS	211 A	2010 January 15	2010 April 17	617.13
		212 A	2009 December 17	2010 May 4	909.90
		532 D	2008 February 8	2010 May 16	−205.87
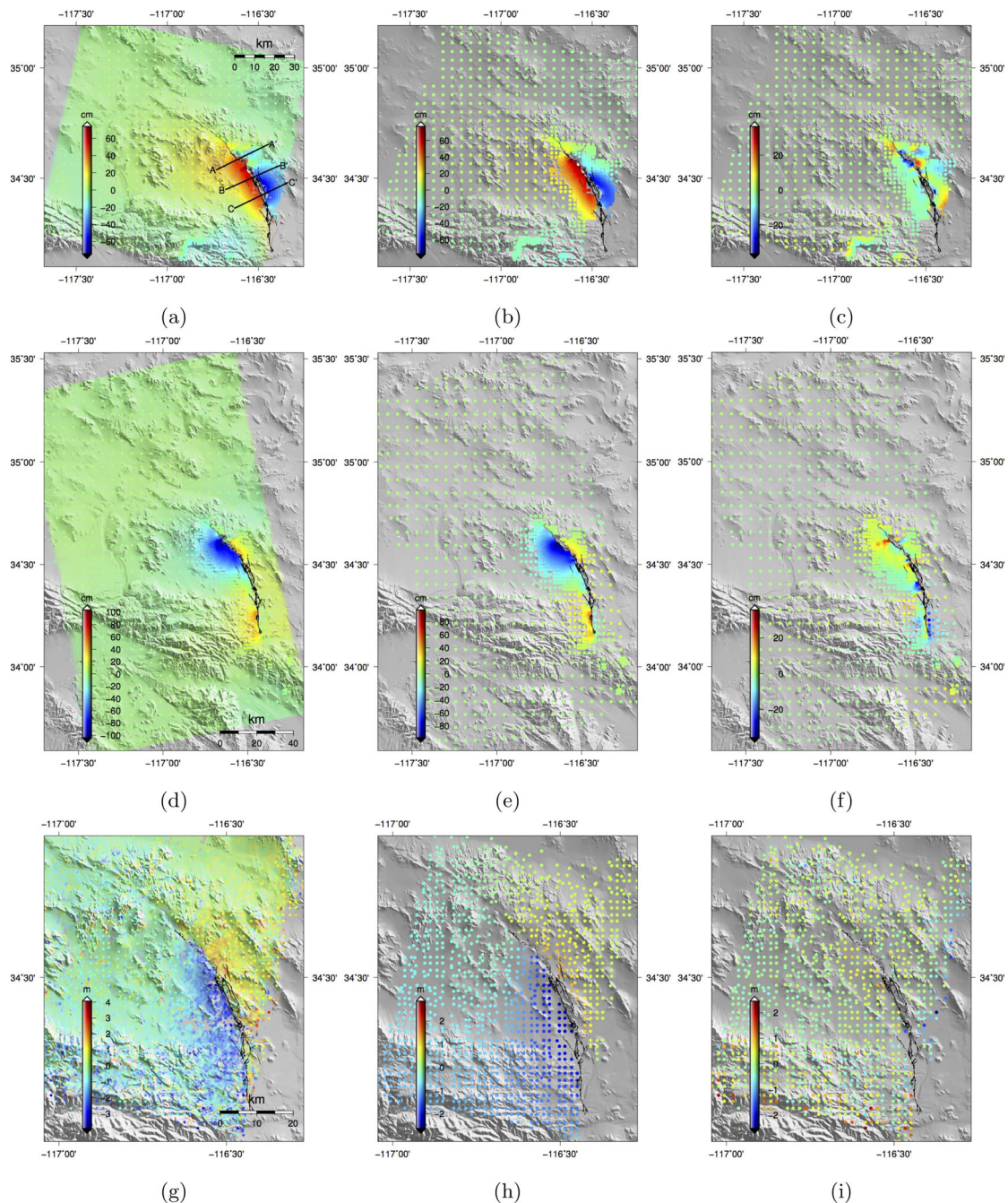
Figure 9. Processed InSAR data, our model prediction and the residual after moving model from data for the 1992 Landers earthquake. (a), (d) and (g) are InSAR unwrapped displacement field from descending track 399, ascending track 349 and the azimuth offset from descending track 399, respectively. (b), (e) and (h) are corresponding model prediction at subsampled data points from (a), (d) and (g), with (c), (f) and (i) being the residuals from fitting.

4 INVERSION

For each of the three earthquakes, we performed joint inversions using the available geodetic data (Table 1) with a uniform elastic half-space model (Simons *et al.* 2002; Tong *et al.* 2010). The In-SAR data provide much of the information for the joint inversions. For each earthquake, we used the best quality data from both ascending and descending look directions. In addition, we used the best-correlated azimuth offsets for each earthquake (Figs 9g, 10g and 11p). These data provide 3-D coverage except close to the fault, where the InSAR correlation is sometimes poor. In these near-fault areas the optical imagery data provide much of the information for

the inversions. We began the modeling by using the fault geometry of published fault models (Simons *et al.* 2002; Fialko 2004; Fialko *et al.* 2010). However, the surface fault traces from these models sometimes conflicted with the more accurate and detailed trace from USGS fault maps. In these cases, we refined the positions of our models' traces following the fault maps. Green's functions, which relate fault slip on a single patch at depth to movement of the ground surface, are computed using an Okada solution (Okada 1992). We assign individual weights for each data set and put them along with the dip angle for each fault segment as non-linear parameters to be inverted for. An optimal solution is given when the parameter search gives less than 0.1 per cent increment in the fitting. The
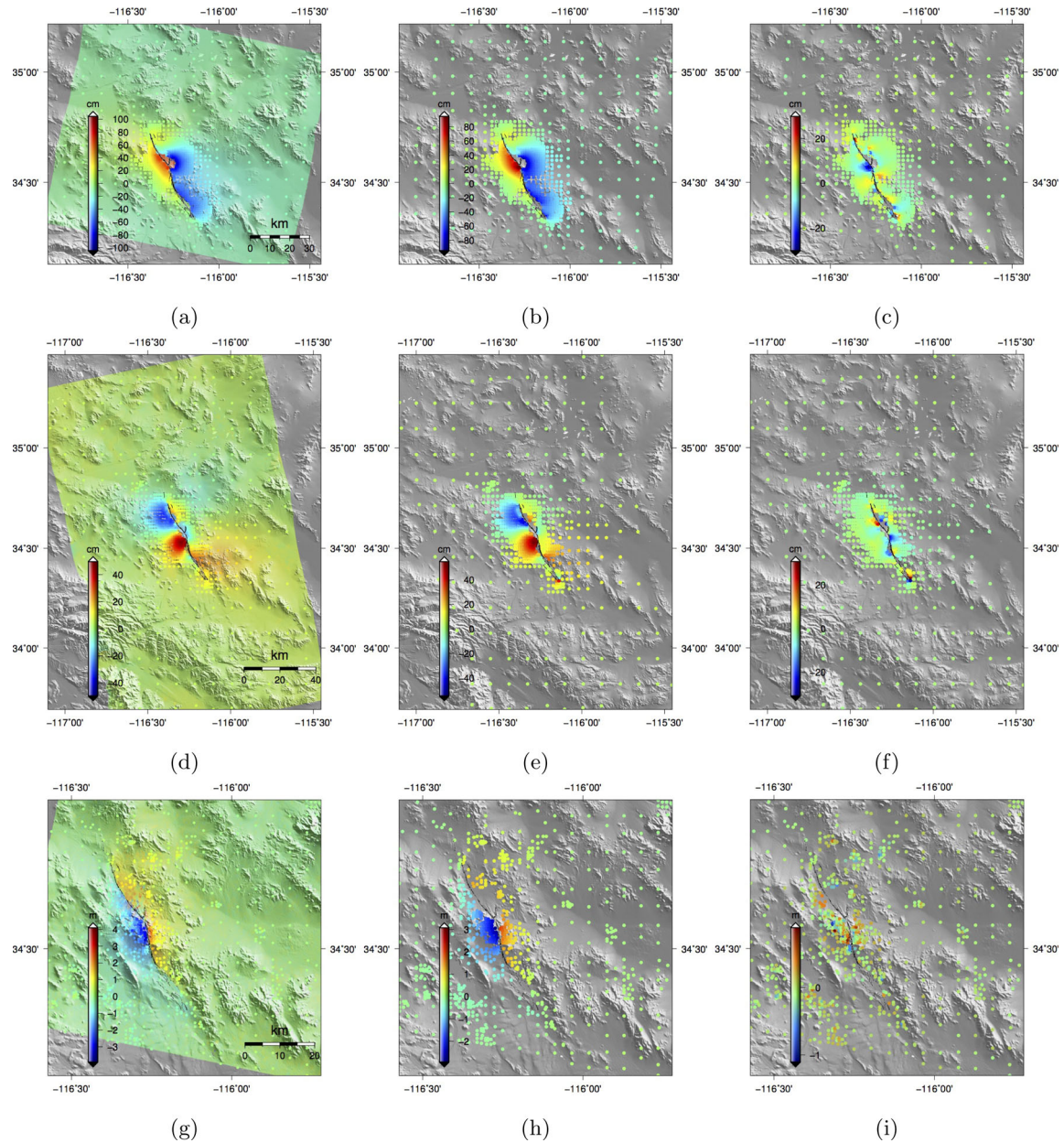
Figure 10. Processed InSAR data, our model prediction and the residual after moving model from data for 1999 Hector Mine earthquake. (a), (d) and (g) are InSAR unwrapped displacement field from descending track 127, ascending track 77 and the azimuth offset from descending track 127, respectively. (b), (e) and (h) are corresponding model prediction at subsampled data points from (a), (d) and (g), with (c), (f) and (i) being the residuals from fitting.

plots of intersections in our model space, along the weights, show the competence between these data sets (Fig. S1). A proper set of weights are given when these data sets are fitted almost equally well. Here, we used the percentage of fitting reduction p instead of absolute rms misfit as a criteria since these data sets have different noise levels and cannot be treated as equally reliable. For example, the azimuth offset data are noisier than the LOS data, so they were downweighted in the inversion. The formula of p is given as

$$p = \left[1 - \frac{(Gm - d)^2}{d^2} \right] \times 100 \text{ per cent}$$

where G is the Green's matrix, m is our model and d is our observation. The inversion solved for the right-lateral strike-slip and dip slip for each segment. A first derivative smoothing operator was applied in order to prevent the model from overfitting. No ex-

tra smoothness along dip was added to keep the fault strike-slip and no bottom or edge damp constraints were set. It is well known that a small change in smoothness factor may cause a large magnitude difference in the slip distribution, as smaller smoothing factor usually gives spiky solution and a larger one may smear this out. Varying this parameter has a strong influence on the estimation of SSD. As is shown in the previous section, our results potentially will give a reduction in the shallow deficit, and in order not to underestimate this deficit (or over reduce it), we try to give less smoothness and do not introduce any other constraints. Again, we used the percentage of reduction as the parameter for selection, because the 'L-curve' method, that is, finding the balanced position between data misfit and model roughness, depends strongly on the scale of plotting, for example, part of the 'L-curve' is still an 'L-curve', but the position of inflection is different. We chose the
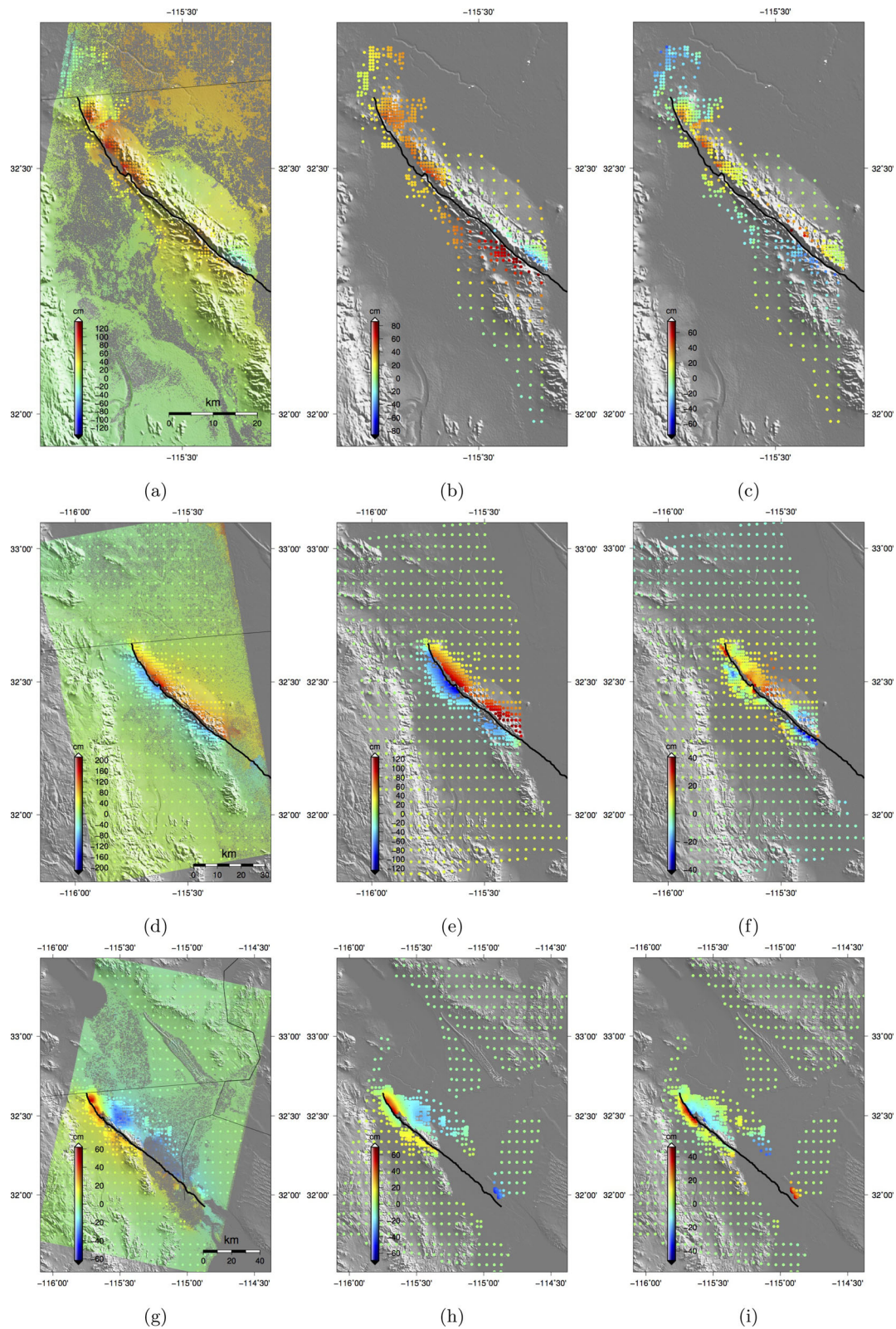
Figure 11. Processed InSAR data, our model prediction and the residual after moving model from data for 2010 El Mayor–Cucapah earthquake. (a), (d), (g), (j), (m) and (p) are InSAR unwrapped displacement field from ALOS descending track 532, ascending track 212, ENVISAT descending track 84, ascending track 77, ascending track 306 and the azimuth offset from ALOS ascending track 212 and 211. (b), (e), (h), (k), (n) and (q) are corresponding model prediction at subsampled data points from (a), (d), (g), (j), (m) and (p), with (c), (f), (i), (l), (o) and (r) being the residuals from fitting, respectively.
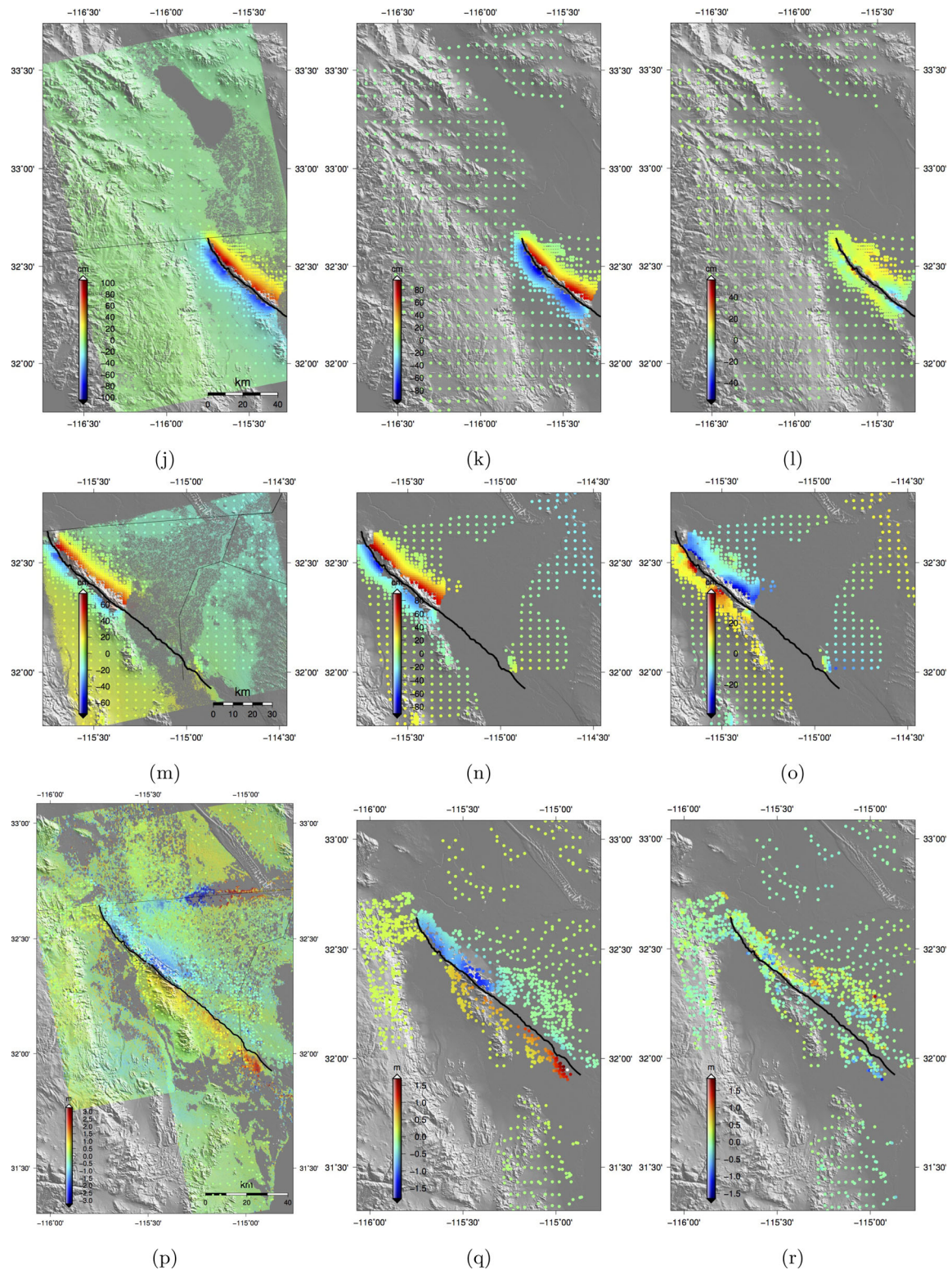
Figure 11. (*Continued.*)

smoothing factor that correspond to the start of decrease in fitting on an absolute scale (Fig. S2, dash line). By doing this, the reduction of the shallow deficit in our analysis can be considered as the minimum.

From these results, we conclude that incorporating the near-fault offset measurements results in better resolution in the shallower part

of the inversion model. Interestingly, for this weighted least-squares process, the weight of the COSI-Corr, near-fault data set showed an independence from other data sets, which means a reasonable weight decrease or increase (before this causes numerical instability) on this data set does not significantly sacrifice the fitting of other data sets (Fig. S1). This unexpected independence not only
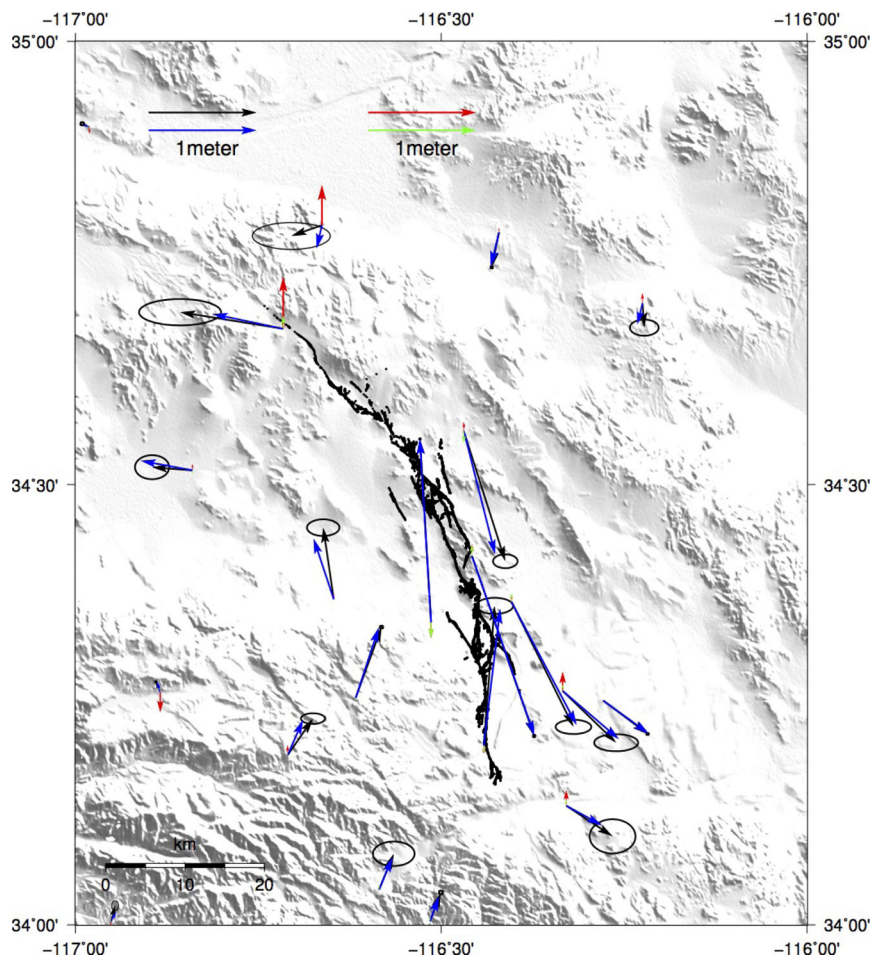
Figure 12. GPS measurements from 82 stations and the forwarded displacement at these stations for 1992 Landers earthquake. Black and red arrows represent horizontal and vertical measurements from GPS and blue and green arrows are forwarded horizontal and vertical displacements from our model. Only near-field stations are plotted.

proves the importance of including near-fault displacement measurements, but also highlights the possible uncertainties in previous inversion studies that lack this type of near-fault surface deformation constraint.

Our reanalysis shown in Figs 15–17, also provides refined equivalent moment–magnitude estimates of 7.3 for the Landers earthquake, 7.1 for the Hector Mine earthquake and 7.2 for the El Mayor–Cucapah earthquake, assuming a typical value for the shear modulus of the Earth's crust (30 GPa). These results agree well with the seismological GCMT (Dziewonski *et al.* 1981) solution. The main new features of our reanalysed models provided more accurate shallow slip estimates due to the addition of the near-fault data. When we integrated along strike, the new cumulative strike-slip versus depth (Fig. 18) shows SSDs ranging from 3 to 18 per cent, which are much smaller than previous studies. Nevertheless, in all three cases the near-fault data require the surface slip to be lower than the modeled slip in the 4–6 km depth range. As discussed below, however, we suspect that much, or even all, of these remaining small SSDs may be more likely to be artefacts of inversion.

5 DISCUSSION

Previous models of three large-magnitude strike-slip earthquakes based on high-quality geodetic data all yielded a deficit of coseismic slip on the uppermost few kilometres of the fault; this was

attributed to a velocity strengthening behaviour in the shallowest part of the crust. The discrepancy in slip at the surface compared to that at depth suggested by the earlier models ranged up to several metres, which is much larger than could be compensated for by other seismic or aseismic mechanisms (Fialko *et al.* 2005). This result not only brought challenges to theoretically explaining the earthquake cycle process but also introduced concerns that surface slip measurement might not be representative of slip at seismogenic depths. If true, this would suggest the underestimation of fault slip rate, with commensurate underestimation of probabilistic seismic hazard (Brune & Anooshehpoor 1998; King & Wesnousky 2007; Hollingsworth *et al.* 2012). Kaneko & Fialko (2011) demonstrated from dynamic rupture simulations that inelastic off-fault deformation could, at most, account for a 15 per cent shallow deficit. Moreover, they showed that, because using purely elastic models may underestimate the true near-surface slip by an additional 10 per cent, consideration of both factors could explain SSDs of as much as 25 per cent. Although this can explain much of the observed SSDs, the artefacts arising from these factors, by themselves, are not sufficient for explaining the very large SSDs observed for the Landers and the El Mayor–Cucapah earthquakes. Here, by introducing detailed near-fault surface deformation data and more accurate representations of the fault surface geometries, we generated more robust estimation of coseismic slip inversions, as well as refined estimates of the magnitude of the surface slip deficits. Specifically, we found
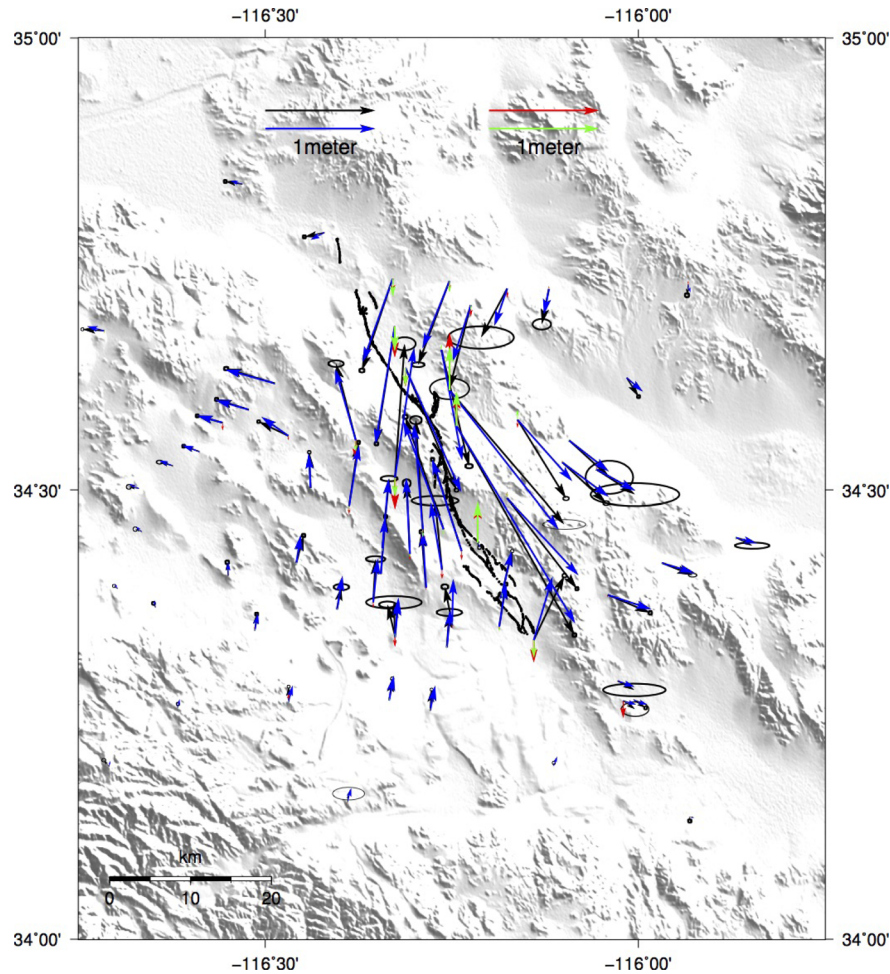
Figure 13. GPS measurements from 77 stations and the forwarded displacement at these stations for 1999 Hector Mine earthquake. Black and red arrows represent horizontal and vertical measurements from GPS and blue and green arrows are forwarded horizontal and vertical displacements from our model. Only near-field stations are plotted.

a significant reduction of the discrepancy between slip at the surface and that at depth for all three large strike-slip earthquakes that we studied, with the shallow deficit for Landers Earthquake being reduced from 46 to 18 per cent, Hector Mine from 18 to 3 per cent and El Mayor–Cucapah from 60 to 11 per cent. These results are consistent with our synthetic tests, which showed that the increased data coverage would lead to a more accurate fault slip model.

Some previous studies of major earthquakes showed only minor residuals after inversion (Jónsson *et al.* 2002; Simons *et al.* 2002; Fialko 2004). In contrast, our study shows that, after performing the inversion, large residuals still exist around the immediate vicinity of the fault. Part of the reason is that we used more near-fault data that have larger error. Also, we need to note the fact that a simplified fault geometry, as used in most inversions, is unable to represent a complicated surface rupture, we believe these large residuals mostly come from near-fault inelastic deformation, even though it could be argued that they may be associated with unwrapping errors. The good correspondence between our unwrapped phase and the fault offset estimates, however, gives us more confidence in the phase unwrapping results. An additional consideration in documenting the SSD is that elastic models may overestimate slip at about 4 km depth, if the true condition is elastoplastic (Kaneko & Fialko 2011). Thus, our estimates of SSD ranging from 3 to 18 per cent may still

overestimate the deficits in these earthquakes, suggesting that the true deficits may be even smaller, or close to zero.

Field surveys of large-magnitude surface ruptures commonly show wide variability in structural style and the variability of on-fault versus off-fault deformation. For example, along many surface ruptures, particularly those on faults with small cumulative displacements (i.e. structurally immature faults) and at major structural complexities along more-mature faults, it is revealed that some fault sections exhibit zones of widely distributed surface deformation that encompass numerous small secondary structures (e.g. minor fault strands and distributed cracking), as well as truly distributed deformation, such as folding and waping (Rockwell *et al.* 2002; Treiman *et al.* 2002; Dolan & Haravitch 2014). Collectively, these structures accommodate distributed inelastic deformation in the near-surface region around the main fault rupture. The style, magnitude and width of these zones of inelastic damage vary from rupture to rupture, likely in response to numerous factors, including the structural maturity of the fault, the detailed structural geometry of the surface rupture and the type and thickness of near-surface geological materials through which the ruptures propagates (Dolan & Haravitch 2014). In the 1999 Hector Mine earthquake, for example, the sections of the rupture that extended the surface in bedrock (Treiman *et al.* 2002) exhibited a relatively small
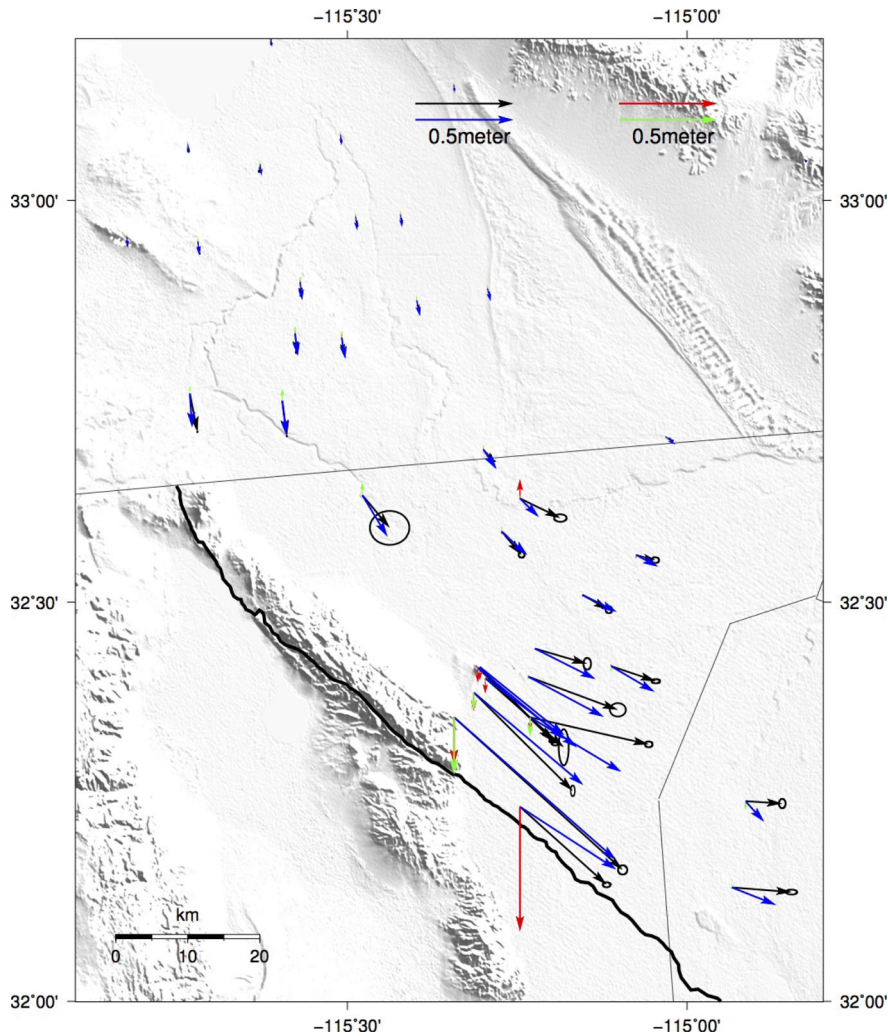
Figure 14. GPS measurements from 158 stations and the forwarded displacement at these stations for 2010 El Mayor–Cucapah earthquake. Black and red arrows represent horizontal and vertical measurements from GPS and blue and green arrows are forwarded horizontal and vertical displacements from our model. Only near-field stations are plotted.

discrepancy between geological surface displacements and estimates of slip at depth from geodetically constrained inversions (Jónsson *et al.* 2002; Simons *et al.* 2002), indicating relatively minor amounts of near-fault inelastic deformation. Conversely, sections of the rupture that extended to the surface through thick sediments showed a much larger discrepancy between on-fault surface displacements and slip at depth from the inversions (Dolan & Haravitch 2014). These very different surface deformation patterns along different parts of the Hector Mine rupture are consistent with the fact that the section of the surface rupture that ruptured through bedrock exhibited only a small decorrelated area near the fault, despite the large magnitude of the earthquake and the interferogram for this event is usually considered to be the best earthquake interferogram yet determined for a major earthquake. In marked contrast, the 2010 $M_w = 7.1$ Darfield earthquake exhibited almost no discrete faulting as part of the surface rupture, despite overall displacements at the surface reaching 5 m (Van Dissen *et al.* 2011). Rather, the surface deformation was expressed as 30- to 300-m-wide zones of distributed faulting, likely as a result of the fact that the rupture extended upwards through very thick, undeformed glacial outwash gravels (Van Dissen *et al.* 2011). Dolan & Haravitch (2014) systematically analysed the discrepancy between geological surface

displacements and estimates of slip from geodetic slip inversion for six large ($M_w = 7.1–7.9$) strike-slip earthquakes and argued that patterns of near-surface inelastic off-fault deformation are controlled to a large degree by the structural maturity of the fault. They found that ruptures on structurally immature faults are characterized by large SSDs, whereas ruptures along structurally mature faults exhibited much small discrepancies between surface fault slip and slip at depth. As discussed above, we can explain most, and perhaps all, of the apparent SSDs for the three earthquakes we studied through a combination of three factors: (1) failure to include constraints on near-fault surface deformation patterns in the inversions; (2) failure to incorporate measurements of distributed (i.e. 'off-fault') inelastic near-surface deformation in the inversions and (3) the use of elastic models, which will underestimate near-surface slip. The three earthquakes we study were all generated by structurally immature faults, and thus exhibited large amounts of near-surface inelastic deformation, and commensurately large apparent SSDs. Earthquakes generated by more structurally mature faults exhibit much smaller apparent SSDs (Dolan & Haravitch 2014), and we think that the factors mentioned above will likely be able to account for all of the measured SSDs, although this remains an area that needs to be documented more thoroughly. In summary, based on these various
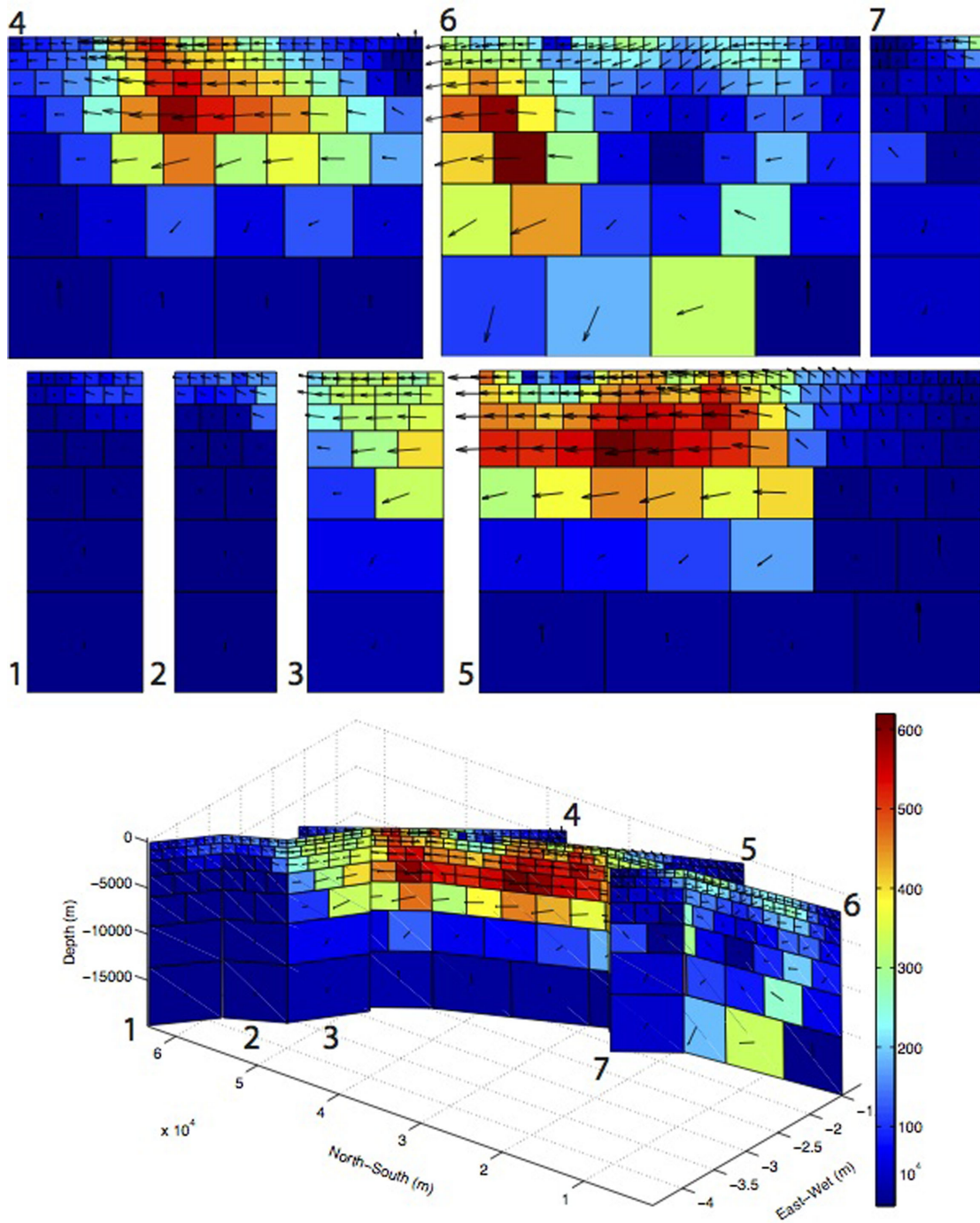
Figure 15. Slip distribution from InSAR-GPS-Arial Image joint inversion for 1992 Landers earthquake with an elastic half-space model. Colours represent strike-slip while arrows stand for total slip and the direction.

factor, we think that most, and perhaps all, of the SSDs that have been inferred in the past can be explained by coseismic inelastic behaviours and will be easily compensated interseismically, if there is any.

6 CONCLUSIONS

We investigated the SSD of three $M_w > 7$ strike-slip earthquakes using GPS and InSAR observations and optical image correlation of aerial photography and SPOT satellite data. Our synthetic test demonstrated that failure to include data on surface deformation around fault may introduce an artificial SSD to elastic half-space models. By exploring the optimal set of the phase unwrapping parameters inside the SNAPHU algorithm, we were able to recover deformation signals that were previously buried in the decorrelated sections of interferograms in the high-deformation zones surrounding the faults. Combining this deformation with additional GPS coverage and near-fault measurements of surface deformation
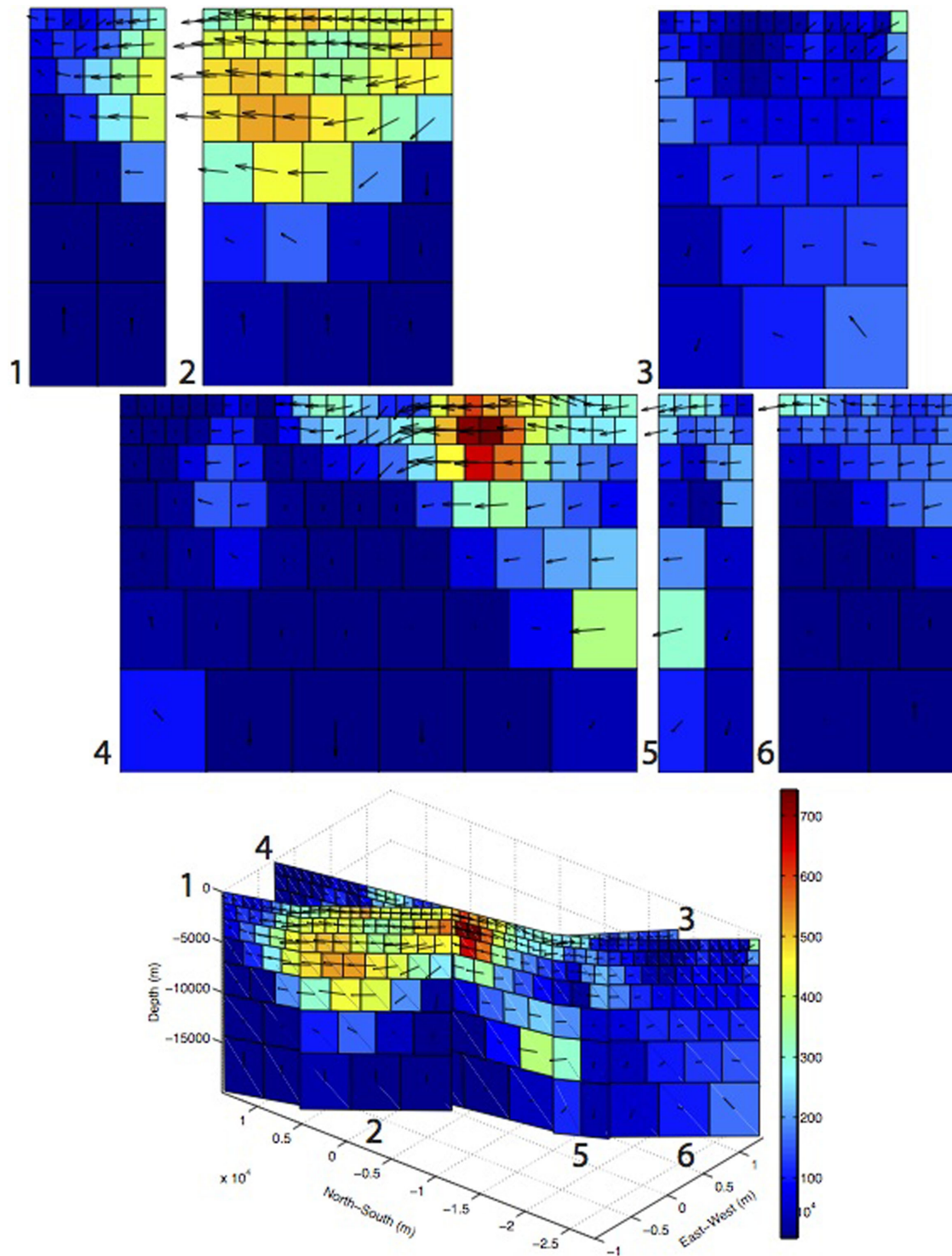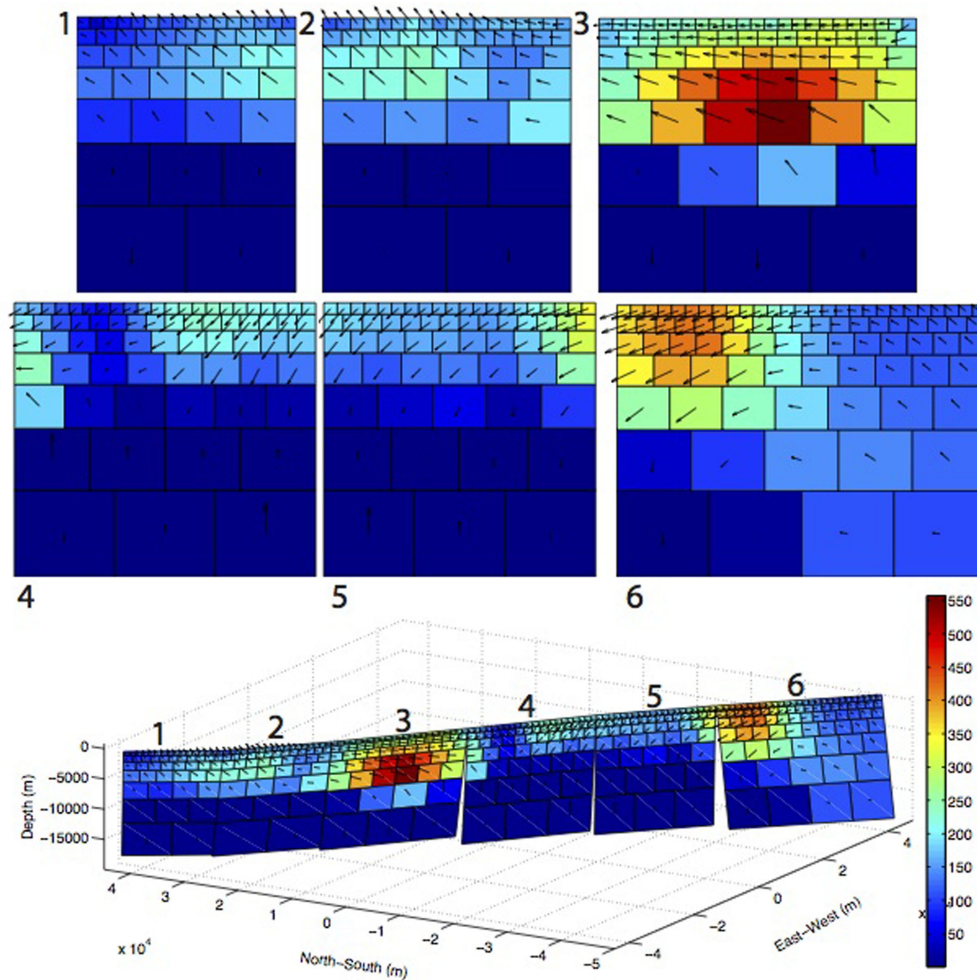
Figure 16. Slip distribution from InSAR-GPS-Arial Image joint inversion for 1999 Hector Mine earthquake with an elastic half-space model. Colours represent strike-slip while arrows stand for total slip and the direction.

patterns from analysis of optical imagery, we provided a spatially complete constraint on the slip versus depth patterns. The resulting inversions reveal relatively small apparent SSDs ranging from 3 to 18 per cent. Although these deficits are much smaller than previous estimates, the left discrepancies need to be explained. We suggest that there are three complementary possible explanations, which are, sample of earthquakes being not large enough, interseismic slip or triggered slip compensation and possibly the artefact from using purely elastic models. The SSDs that have been apparent in previous comparisons of on-fault geological are at least partially, and perhaps almost entirely, artefacts of the earlier analyses. Failure to incorporate near-fault surface deformation patterns as a constraint in geodetic inversions, together with a smoothness regularization, can lead to artificial SSDs that obscure the fact that essentially all slip at depth in large earthquakes likely extends to the surface as a combination of on-fault slip and off-fault distributed deformation.

Figure 17. Slip distribution from InSAR-GPS-Arial Image joint inversion for 2010 El Mayor–Cucapah earthquake with an elastic half-space model. Colours represent strike-slip while arrows stand for total slip and the direction.
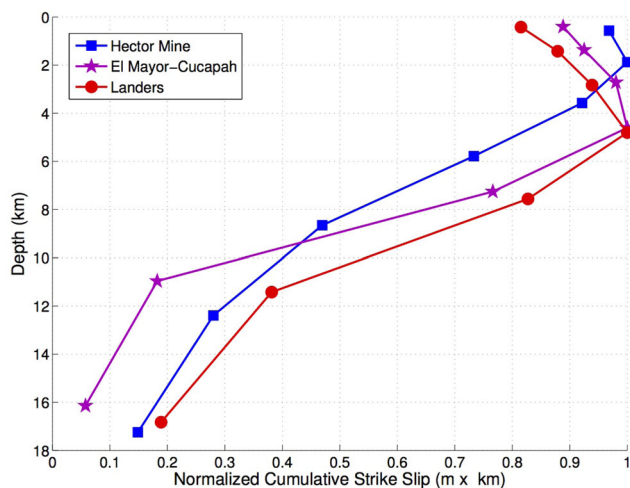
Figure 18. Normalized cumulative strike-slip versus depth for three large strike-slip earthquakes, from our new inversion results. Cumulative strike-slip is computed by integrating the strike-slip along fault trace. The results are normalized by the maximum amount of cumulative strike-slip.

REFERENCES

Agnew, D.C., Owen, S., Shen, Z.-K., Anderson, G., Svarc, J., Johnson, H., Austin, K.E. & Reilinger, R., 2002. Coseismic displacements from the Hector Mine, California, earthquake: results from survey-mode global positioning system measurements, *Bull. seism. Soc. Am.,* **92**(4), 1355–1364.

Ayoub, F., Leprince, S. & Avouac, J.-P., 2009. Co-registration and correlation of aerial photographs for ground deformation measurements, *ISPRS J. Photogramm. Remote Sens.,* **64**(6), 551–560.

Bock, Y. *et al.*, 1993. Detection of crustal deformation from the Landers earthquake sequence using continuous geodetic measurements, *Nature,* **361**(6410), 337–340.

Brune, J.N. & Anooshehpoor, A., 1998. A physical model of the effect of a shallow weak layer on strong ground motion for strike-slip ruptures, *Bull. seism. Soc. Am.,* **88**(4), 1070–1078.

Chen, C.W. & Zebker, H.A., 2001. Two-dimensional phase unwrapping with use of statistical models for cost functions in nonlinear optimization, *J. Opt. Soc. Am. A,* **18**(2), 338–351.

Dolan, J.F. & Haravitch, B.D., 2014. How well do surface slip measurements track slip at depth in large strike-slip earthquakes? The importance of fault structural maturity in controlling on-fault slip versus off-fault surface deformation, *Earth planet. Sci. Lett.,* **388,** 38–47.

Dziewonski, A., Chou, T.-A. & Woodhouse, J., 1981. Determination of earthquake source parameters from waveform data for studies of global and regional seismicity, *J. geophys. Res.,* **86**(B4), 2825–2852.

Fialko, Y., 2004. Probing the mechanical properties of seismically active crust with space geodesy: study of the coseismic deformation due to the 1992 M_w 7. 3 Landers (southern California) earthquake, *J. geophys. Res.,* **109**(B3), doi:10.1029/2003JB002756.

Fialko, Y., Simons, M. & Agnew, D., 2001. The complete (3-d) surface displacement field in the epicentral area of the 1999 M_w 7. 1 Hector Mine earthquake, California, from space geodetic observations, *Geophys. Res. Lett.,* **28**(16), 3063–3066.

Fialko, Y., Sandwell, D., Simons, M. & Rosen, P., 2005. Three-dimensional deformation caused by the Bam, Iran, earthquake and the origin of shallow slip deficit, *Nature,* **435**(7040), 295–299.

Fialko, Y., Gonzalez, A., Gonzalez, J., Barbot, S., Leprince, S., Sandwell, D. & Agnew, D., 2010. Static rupture model of the 2010 *M*7.2 El Mayor-Cucapah earthquake from ALOS, ENVISAT, SPOT and GPS data, *EOS, Trans. Am. geophys. Un.,* **91**(52), T53B–2125.

Hollingsworth, J., Dolan, J.F., Milliner, C.W., Leprince, S., Ayoub, F. & Avouac, J., 2012. Analysis of the shallow slip deficit using sub-pixel image correlation: implications for fault slip rates, and seismic hazards, in *AGU Fall Meeting Abstracts,* American Geophysical Union, Abstract #T23H-02.

Huang, Y.H. & Van Genderen, J.L., 1997. Comparison of several multi-look processing procedures in INSAR processing for ERS-1&2 tandem mode, *ERS SAR Interferometry,* **406,** 215–221.

Jónsson, S., Zebker, H., Segall, P. & Amelung, F., 2002. Fault slip distribution of the 1999 M_w 7.1 Hector Mine, California, earthquake, estimated from satellite radar and GPS measurements, *Bull. seism. Soc. Am.,* **92**(4), 1377–1389.

Kaneko, Y. & Fialko, Y., 2011. Shallow slip deficit due to large strike-slip earthquakes in dynamic rupture simulations with elasto-plastic off-fault response, *Geophys. J. Int.,* **186**(3), 1389–1403.

Kaneko, Y., Hamling, I., Van Dissen, R., Motagh, M. & Samsonov, S., 2015. InSAR imaging of displacement on flexural-slip faults triggered by the 2013 M_w 6.6 Lake Grassmere earthquake, central New Zealand, *Geophys. Res. Lett.,* **42**(3), 781–788.

King, G.C. & Wesnousky, S.G., 2007. Scaling of fault parameters for continental strike-slip earthquakes, *Bull. seism. Soc. Am.,* **97**(6), 1833–1840.

Leprince, S., Barbot, S., Ayoub, F. & Avouac, J.-P., 2007. Automatic and precise orthorectification, coregistration, and subpixel correlation of satellite images, application to ground deformation measurements, *IEEE Trans. Geosci. Remote Sens.,* **45**(6), 1529–1558.

Massonnet, D., Rossi, M., Carmona, C., Adragna, F., Peltzer, G., Feigl, K. & Rabaute, T., 1993. The displacement field of the Landers earthquake mapped by radar interferometry, *Nature,* **364**(6433), 138–142.

Massonnet, D., Feigl, K., Rossi, M. & Adragna, F., 1994. Radar interferometric mapping of deformation in the year after the Landers earthquake, *Nature,* **369**(6477), 227–230.

Michel, R. & Avouac, J.-P., 2006. Coseismic surface deformation from air photos: the Kickapoo step over in the 1992 Landers rupture, *J. geophys. Res.,* **111**(B3), doi:10.1029/2005JB003776.

Milliner, C.W.D., Dolan, J.F., Hollingsworth, J., Leprince, S., Ayoub, F. & Sammis, C.G., 2015. Quantifying near-field and off-fault deformation patterns of the 1992 M_w 7.3 Landers earthquake, *Geochem. Geophys. Geosyst.,* **16**(5), 1577–1598.

Okada, Y., 1992. Internal deformation due to shear and tensile faults in a half-space, *Bull. seism. Soc. Am.,* **82**(2), 1018–1040.

Pitarka, A., Dalguer, L.A., Day, S.M., Somerville, P.G. & Dan, K., 2009. Numerical study of ground-motion differences between buried-rupturing and surface-rupturing earthquakes, *Bull. seism. Soc. Am.,* **99**(3), 1521–1537.

Reid, H.F., 1910. *The California Earthquake of April 18, 1906: Report of the State Earthquake Investigation Commission*; Vol. 2, 32 pp., Carnegie Institution of Washington, Washington, DC.

Rice, J.R. & Tse, S.T., 1986. Dynamic motion of a single degree of freedom system following a rate and state dependent friction law, *J. geophys. Res.,* **91**(B1), 521–530.

Rockwell, T.K., Lindvall, S., Dawson, T., Langridge, R., Lettis, W. & Klinger, Y., 2002. Lateral offsets on surveyed cultural features resulting from the 1999 Izmit and Düzce earthquakes, turkey, *Bull. seism. Soc. Am.,* **92**(1), 79–94.

Sandwell, D.T. & Price, E.J., 1998. Phase gradient approach to stacking interferograms, *J. geophys. Res.,* **103**(B12), 30 183–30 204.

Simons, M. & Rosen, P.A., 2007. Interferometric synthetic aperture radar geodesy, in *Treatise on Geophysics,* Vol. 3, pp. 391–446, ed. Schubert, G., Elsevier.

Simons, M., Fialko, Y. & Rivera, L., 2002. Coseismic deformation from the 1999 M_w 7.1 Hector Mine, California, earthquake as inferred from InSAR and GPS observations, *Bull. seism. Soc. Am.,* **92**(4), 1390–1402.

Tong, X., Sandwell, D.T. & Fialko, Y., 2010. Coseismic slip model of the 2008 Wenchuan earthquake derived from joint inversion of interferometric synthetic aperture radar, GPS, and field data, *J. geophys. Res.,* **115**(B4), doi:10.1029/2009JB006625.

Treiman, J.A., Kendrick, K.J., Bryant, W.A., Rockwell, T.K. & McGill, S.F., 2002. Primary surface rupture associated with the M_w 7.1 16 October 1999 Hector Mine earthquake, San Bernardino County, California, *Bull. seism. Soc. Am.,* **92**(4), 1171–1191.

Tse, S.T. & Rice, J.R., 1986. Crustal earthquake instability in relation to the depth variation of frictional slip properties, *J. geophys. Res.,* **91**(B9), 9452–9472.

Van Dissen, R. *et al.*, 2011. Surface rupture displacement on the Greendale fault during the M_w 7.1 Darfield (Canterbury) earthquake, New Zealand, and its impact on man-made structures, in *Proceedings Ninth Pacific Conference on Earthquake Engineering,* Building an Earthquake-Resilient Society, Auckland, New Zealand, 14–16 April 2011, New Zealand Society for Earthquake Engineering, Paper 186, 8 pp.

Wei, M., Sandwell, D. & Fialko, Y., 2009. A silent M_w 4.7 slip event of October 2006 on the Superstition Hills fault, southern California, *J. geophys. Res.,* **114**(B7), doi:10.1029/2008JB006135.

Zebker, H.A., Rosen, P.A., Goldstein, R.M., Gabriel, A. & Werner, C.L., 1994. On the derivation of coseismic displacement fields using differential radar interferometry: the Landers earthquake, *J. geophys. Res.,* **99**(B10), 19 617–19 634.

Zhang, H., Thurber, C. & Bedrosian, P., 2009. Joint inversion for Vp, Vs, and Vp/Vs at SAFOD, Parkfield, California, *Geochem. Geophys. Geosyst.,* **10**(11), doi:10.1029/2009GC002709.

SUPPORTING INFORMATION

Additional Supporting Information may be found in the online version of this paper:

Figure S1. Cross-sections in model space along weigh directions versus percentage of recovery. Horizontal axes for (a) (b) and (c) represents weighs of azimuth offset, GPS observations and fault offset estimates from SPOT image, for the inversion of 1992 Landers earthquake, while weigh for InSAR phase data is defined as 1. Similarly, (d), (e) and (f) are weighs of the datasets for 1999 Hector Mine earthquake and (g), (h) and (i) for 2012 El Myaor-Cucapah earthquake. In all the plots above, blue line represents the recovery for InSAR phase data, red line for InSAR azimuth offset data, green line for the recovery of GPS data and magenta line for the

recovery of estimated fault offset from aerial image. Grey dash lines represents the selection of the weigh values.

Figure S2. Percentage of recovery for each dataset versus smooth factor in each inversion. (a) 1992 Landers, (b) 1999 Hector Mine, (c) 2010 El Mayor-Cucapah. In all the plots above, blue line represents the recovery of InSAR phase data, red line for the recovery InSAR azimuth offset data, green line for the recovery of GPS data, magenta line for the recovery of estimated fault offset from aerial image and black line represents the mean recovery of these four data sets. Grey dash lines represent the selection of smooth factor for each earthquake.

Figure S3. How to correctly unwrap a deformation field with a rupture inside. (a) is the true deformation field in radiant (phase). (b) is the wrapped phase, i.e. the synthetic interferogram. (c) is the directly unwrapped phase using SNAPHU with default settings. (d) is the unwrapped phase with a correlation mask right on the rupture. (e) is unwrapped phase with assuming a maximum discontinuity being approximately 400 radiant. (f) is unwrapped phase with combing methods in (d) and (e), i.e. assuming an approximate maximum discontinuity and setting a correlation mask on fault.

Figure S4. Synthetic test of inversion with full data coverage. (a) is the North component of the deformation field with assumed slip in Fig. 3(a). (b) is the recovered slip from inversion with 2 per cent local noise added. (c) is the cumulative strike slip versus depth with the dash line being the input slip from Fig. 3(a).

Figure S5. Monte Carlo simulation for testing the model's uncertainty by perturbing the data with spatially correlated red noise (1000 realizations). (a) is an example of the red noise generated for each InSAR scene during each realization. (b) and (c) are the strike-slip and dip-slip uncertainty for the 1992 Landers earthquake in cm. (d) and (e) are the strike-slip and dip-slip uncertainty for the 1999 Hector Mine earthquake in cm. (f) and (g) are the strike-slip and dipslip uncertainty for the 2010 El Mayor-Cucapah earthquake in cm (http://gji.oxfordjournals.org/lookup/suppl/doi:10.1093/gji/ggv563/-/DC1).

Please note: Oxford University Press is not responsible for the content or functionality of any supporting materials supplied by the authors. Any queries (other than missing material) should be directed to the corresponding author for the paper.

APPENDIX: JOINT INVERSION PROCEDURE

Here, we provide the inversion procedure used to estimate slip at depth from a variety of surface observations. The overall approach is to minimize the misfit between the observations and the model subject to positivity and smoothness constraints. The minimization is

$$\min(||Am - b||^2 + \lambda^2 ||Sm||^2) \tag{A1}$$

where λ is the smoothness factor that represent how rough the slip distribution is. $Am = b$ together with $Sm = 0$, can be expanded as following

$$\begin{bmatrix} W_p G_p & W_p W_r R_p \\ W_a G_a & W_a W_r R_a \\ W_g G_g & 0 \\ W_o G_o & 0 \\ \lambda S & 0 \end{bmatrix} \begin{bmatrix} m_u \\ m_r \end{bmatrix} = \begin{bmatrix} W_p d_p \\ W_a d_a \\ W_g d_g \\ W_o d_o \\ 0 \end{bmatrix} \tag{A2}$$

where G are the Green's functions calculated according to Okada (1992), with three components being projected to observation directions for InSAR and GPS data, and to the fault azimuth for optical

imagery data. d represent observations, W represent weighs (here are diagonal matrices), R represent orbital error absorbing components, S represent smoothness regularization and m is the model. Subscripts p, a, g and o refer to InSAR phase, InSAR azimuth offset, GPS and optical imagery data, respectively. Subscript r refers to ramp absorbing component and u refers to modeled slip. Other non-linear parameters such as dipping angles are included in the computation of Green's function (Okada 1992).

For the weighs of each data set, they are the multiplication of two parts, the pre-assigned weigh w_{pre} and the weigh relative to InSAR phase data w_{post}. For InSAR data, w_{pre} is proportional to the square root of the number of points inside a subsampled section (n_i) (Simons *et al.* 2002), which is

$$w_{\mathrm{pre}}^i = \frac{n_i^{1/2}}{\sum_{j=1}^N n_j^{1/2}} \tag{A3}$$

where N is the total number of points in each data set. For GPS and optical imagery data, w_{pre} is inversely proportional to the uncertainty (σ_i) (Simons *et al.* 2002), which is

$$w_{\mathrm{pre}}^i = \frac{\sigma_i^{-1}}{\sum_{j=1}^M \sigma_j^{-1}} \tag{A4}$$

where M is the total number of observations in each data set. The weighs relative to InSAR phase data w_{post} are part of the non-linear parameters we established a comprehensive search for (solutions shown in Fig. S1).

The orbital ramp components are composed of columns of x, y positions and ones for representing individual planar ramps for each InSAR acquisition as following.

$$\begin{bmatrix} R_p \\ R_a \end{bmatrix} = \begin{bmatrix} x_1^1 & y_1^1 & 1 & 0 & 0 & 0 & 0 & 0 & 0 & \dots \\ x_2^1 & y_2^1 & 1 & 0 & 0 & 0 & 0 & 0 & 0 & \dots \\ \dots & \dots & \dots & \dots & \dots & \dots & \dots & \dots & \dots & \dots \\ 0 & 0 & 0 & x_1^2 & y_1^2 & 1 & 0 & 0 & 0 & \dots \\ 0 & 0 & 0 & x_2^2 & y_2^2 & 1 & 0 & 0 & 0 & \dots \\ \dots & \dots & \dots & \dots & \dots & \dots & \dots & \dots & \dots & \dots \\ 0 & 0 & 0 & 0 & 0 & 0 & x_1^3 & y_1^3 & 1 & \dots \\ 0 & 0 & 0 & 0 & 0 & 0 & x_2^3 & y_2^3 & 1 & \dots \\ \dots & \dots & \dots & \dots & \dots & \dots & \dots & \dots & \dots & \dots \end{bmatrix} \tag{A5}$$

where x and y represent east and north positions. In x_j^i, i and j refer jth point in ith acquisition. After the inversion, each ramp signal can be estimated as $r_j^i = a_i x_j^i + b_i y^i + c_i$, where a_i, b_i and c_i are parameters in m_r. Also, in order to get a robust solution for both the ramp and the slip model, we began the inversion with a relatively high ramp weigh (W_r). After removing this initial ramp from the data, we assign a smaller weigh (W_r) so as to remove any remaining residual ramp while not affecting the solution of the slip.

Since we assumed the faults having both strike and dip slip during the earthquakes, the model is represented as

$$\begin{bmatrix} m_u \\ m_r \end{bmatrix} = \big(s_1^s, s_1^d, s_2^s, s_2^d, \dots \quad \dots s_N^s, s_N^d,$$
$$a_1, b_1, c_1, \dots \quad \dots a_M, b_M, c_M\big)^T \tag{A6}$$

where s_i^s and s_i^d represent strike and dip slip for the ith patch, and a_i, b_i and c_i are ramp parameters for the ith InSAR acquisition. N is

the total number of patches in a model and M is the total number of InSAR acquisitions used in the inversion.

The first difference smoothness matrix is given by

$$
S = \begin{bmatrix}
\cdots & \cdots & \cdots & \cdots & \cdots & \cdots \\
\cdots & -1/r_{ij} & \cdots & 1/r_{ij} & \cdots & \cdots \\
\cdots & \cdots & -1/r_{ij} & \cdots & 1/r_{ij} & \cdots \\
\cdots & \cdots & \cdots & \cdots & \cdots & \cdots
\end{bmatrix}
\tag{A7}
$$

where i and j are indexes of two adjacent patches and r represent the distance between the two patches. Note that the smoothness are the same for dip and strike slip.

The optimization for non-linear parameters is done by systematically searching the parameter space with one parameter at time. The search exits when no parameter change can provide a 0.1 per cent smaller overall least-squares residual between the model and the data. A series of large-scale initial states are tested in order to avoid the solution from falling into local minima. The Green's functions are recomputed when the fault geometry changes.